Bacterial chemotaxis: a classic example of multiscale modeling in biology

Chuan Xue

1 Introduction

Active cell movement plays a crucial role in the life of living organisms, and in many situations the movement is guided by extracellular chemical signals. Sperm cells swim long distances to fertilize an egg, and this process is directed by chemical substances released from the outer surface of the egg [1]. Neutrophils and fibroblasts move into a wound to stop infection and rebuild the tissue, and this process is orchestrated by a number of chemical signals [2]. Cancer cells can migrate away from a primary tumor to invade other tissues and cause cancer metastasis [3]. In bioremediation, bacteria are used to clean waste water because they migrate towards certain toxins and degrade them [4]. The directed movement of cells or organisms in response to extracellular chemical signals is called "chemotaxis".

To understand the role of chemotaxis in multicellular processes, it is crucial to develop quantitative and predictive mathematical models to describe chemotaxis of cell populations. Detailed individual-based models have been developed to incorporate data in cell signaling, movement, as well as cell-cell interaction. This approach can faithfully replicate the biology, but due to the large number of cells involved and the complexity of the intracellular dynamics, they are computationally intensive and frequently become intractable. Alternatively, simplified PDE models have also been used to describe the spatial-temporal dynamics of the cell densities. This approach is appealing and convenient because of the variety of mathematical tools available in simulation and analysis of PDE models. However, these models often rely on phenomenological assumptions of cell fluxes which cannot be easily justified experimentally. Multiscale methods to embed data at the cellular and sub-cellular processes into PDE models of the cell population dynamics must be developed to combine the strengths of these two approaches.

Chuan Xue
Department of Mathematics, Ohio State University, Columbus, OH 43210, e-mail: cxue@math.osu.edu

Significant progress has been made along this line for bacterial chemotaxis, which is the most basic and best understood form of chemotaxis. In this chapter, I review results that focus on the derivation of PDE models for bacterial chemotaxis from individual-based models that describe single cell movement as a velocity jump process and integrates intracellular signaling as an internal ODE system. Through numerical examples, I illustrate the application scope and limitations of the well-known Patlak-Keller-Segel chemotaxis equation in modeling the bacteria population dynamics. The mathematical framework developed for bacterial chemotaxis can be extended to similar biological systems and serve as a classic example for multiscale modeling in biology.

2 Biological background

Chemotaxis of run-and-tumble bacteria has been extensively studied over the past 50 years. Examples of such bacteria include *Escherichia*, *Salmonella*, *Bacillus*, *Rhodobacter*, and *Pseudomonas* [5, 6, 7, 8]. Among them the best understood is the model system *Escherichia coli* [9, 10, 8], which is described below in detail. Chemotaxis of other bacteria is similar but not identical to that of *E. coli*.

2.1 Single cell movement

E. coli has a cylindrical cell body that is 1-2 μm-long and several helical flagella that project away from the cell body in all directions. Each flagellum can be rotated by a flagellar motor embedded in the cell membrane either clockwise or counterclockwise. If all the flagella are rotated counterclockwise (CCW), they form a single bundle and push the cell forward in a long smooth "run" at a speed $s = 10$ - 30 μm/s; if some flagella are rotated clockwise (CW), these flagella disengage from the bundle causing the cell to stop and "tumble" in place. The cell moves by randomly alternating smooth runs and reorienting tumbles. In the absence of a chemical signal gradient, the mean run time is 1 s and mean tumble time is 0.1 s. However, if the cell is exposed to a signal gradient, it alters the rotation pattern of each flagellar motor so that the run time is extended when the cell moves up (down) the gradient of a chemoattractant (chemorepellent).

2.2 Intracellular signaling

The rotation of a flagellar motor is controlled by the intracellular chemotaxis pathway shown in Figure 1. The transmembrane chemoreceptors form stable ternary complexes with the signaling proteins CheA and CheW, and cluster at one pole

of the cell body. CheA is an auto-kinase, and its activity is reduced if attractant molecules bind to the associated receptor but can be restored if the methylation level of the receptor increases. CheA is also a kinase for the response regulators CheY and CheB. The phosphorylated form CheYp binds to the flagella motor, which increases the probability of CW rotation and triggers tumbling. CheBp and CheR change the methylation state of the receptor at a slower rate: CheR methylates it and CheBp demethylates it.

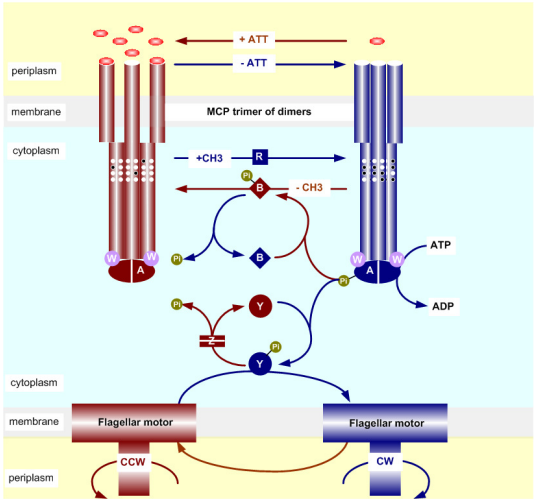

Fig. 1 The chemotaxis signaling pathway for the model bacterium E. coli. Transmembrane chemoreceptors function as trimers of dimers with ligand-binding domains on the peri-plasmic side and signaling domains on the cytoplasmic side. Methylation sites of receptors appear as white dots on the receptors. The cytoplasmic signaling proteins are represented by single letters, e.g., A = CheA. Red (blue) components promote CCW (CW) rotation of flagellar motors. Reprinted from [11] with permission.

Upon ligand binding, the kinase activity of CheA is reduced, thus CheYp decreases rapidly, and the cell tends to run for longer. This process, called excitation, occurs within fractions of seconds. Simultaneously, CheBp is reduced but CheR is not affected, thus the receptor methylation level increases, until the activity of CheA is restored to its pre-stimulus level. This process, called adaptation, takes seconds to minutes, depending on the nature of the signal. We note that excitation and adaptation are two concurrent processes that affect each other, specifically, adaptation acts as a negative feedback to excitation and allows the cell to subtract away background signal and respond to further signal changes.

Bacterial chemotaxis involves multiple time scales. Ligand binding to chemoreceptors on the cell membrane, change of kinase activity, and phosphorylation reactions inside a cell occur within fractions of seconds. Methylation and demethylation of the receptors that cause adaptation of a cell occur on a time scale of seconds. The adaptation time scale is the slowest time scale for intracellular dynamics. It is

intrinsically determined by the intracellular signaling network, and reflects the time scale of methylation and demethylation.

3 Individual-based models

Chemotaxis plays a critical role in self-organization patterns formed in bacterial colonies, e.g., traveling bands, aggregates, swarm rings [12, 13, 14, 15, 16]. To understand the interplay of different mechanisms in the pattern formation process, individual-based models have been developed to couple descriptions of single cell movement (Sec 3.1) and cell signaling (Sec 3.2), as well as cell growth and the dynamics of extracellular signals [17, 18, 19].

When the cell density is sufficiently low, cell-cell mechanical interactions can be neglected and cell movement can be modeled as velocity jump processes without collisions. This situation may still involve a large population of cells. For example, in case that the cell volume fraction is 0.1% and the medium has dimension 1cm $\times$ 1cm $\times$ 1mm, assume that the volume of a single cell is approximately $1\mu m^3$, then the number of cells is approximately 10^8. When the cell density becomes high, cells can also interact with each other through the surrounding fluid. Individual-based models have been developed for such situations by treating cells as particles without intracellular dynamics [20, 21, 22, 23, 24, 25, 26, 27]. Our review focuses on the low cell density situation.

3.1 Single cell movement modeled as a velocity jump process

The run-and-tumble movement of a single cell is frequently modeled as a velocity-jump process [28, 17, 29]. A velocity jump process is a stochastic process in which the velocity of an individual jumps instantaneously at random time points. The velocity jumps can be characterized by two quantities: a turning rate function which specifies when the next velocity jump occurs and a turning kernel which specifies the probability density of the new velocity given the velocity prior to the jump.

3.1.1 A base model

For bacterial chemotaxis, the mean tumble time is much smaller than the mean run time, thus the tumbling phase of the cell movement is usually ignored. The speed of the cell is usually assumed to be constant, and thus the velocity space is a sphere

$$V = s_0 \partial B_0^1, \tag{1}$$

where s_0 is the typical speed of the cell and ∂B_0^1 is the unit sphere centered at the origin.

Under this simplification, the cell movement can be modeled as a sequence of runs connected by instantaneous reorientations. Because CheYp binding suppresses CCW rotation of the flagella which in turn induce tumbling, the turning rate λ is an increasing function of intracellular CheYp concentration y_p, i.e.,

$$\lambda = \lambda(y_p). \tag{2}$$

The turning kernel is usually assumed to only depend on the angle between $\mathbf{v}$ and $\mathbf{v}'$, denoted as θ,

$$T(\mathbf{v},\mathbf{v}') = h(\theta). \tag{3}$$

Recordings of cell trajectories in free space shows that *E. coli* has a slight directional persistence towards the previous direction after a tumble [30, 31], thus $h(\theta)$ is a decreasing function. To conserve probability, one must have

$$\int_V T(\mathbf{v},\mathbf{v}')\mathrm{d}\mathbf{v} = 1. \tag{4}$$

Under the above assumptions, the movement of a single cell is described by the following SDE system

$$\begin{cases} \mathrm{d}\mathbf{x} = \mathbf{v}\mathrm{d}t, \\ \mathrm{d}\mathbf{v} = (\zeta - \mathbf{v})\mathrm{d}Y(t,\lambda), \end{cases} \tag{5}$$

where ζ is a random variable with probability density given by $T(\cdot,\mathbf{v})$ and $Y(t,\lambda)$ is an inhomogeneous Poisson process with intensity given by $\lambda(y_p)$. The system is coupled with equations for cell signaling through the variable y_p.

3.1.2 Inclusion of cell tumbling

More detailed models have been developed to incorporate a finite tumbling phase explicitly. This was achieved by describing the cell movement as a velocity jump process with a moving state and a resting state. Denote the rate for a running cell to stop and tumble by λ and the rate for a tumbling cell to start running by μ, i.e.,

$$\text{Run} \underset{\mu}{\overset{\lambda}{\rightleftharpoons}} \text{Tumble}.$$

The transition rates λ and μ depend on the rotation state of all the flagella around the cell body, which in turn depends on intracellular CheYp concentration y_p. Thus one has

$$\lambda = \lambda(y_p), \qquad \mu = \mu(y_p).$$

The switching behavior of a single flagellum between CW and CCW rotations has been measured under different CheYp concentrations in [32]. Specifically, ex-

perimental data was collected on the CW bias (P_{CW}) and the switching frequency (F) of a single flagellar motor (Fig. 2A-B, dots), which revealed the ultrasensitivity of the motor to CheYp.

Assume the direction switches between CCW and CW are first order reactions with rates λ_f and μ_f, i.e.,

$$\text{CCW} \underset{\mu_f}{\overset{\lambda_f}{\rightleftharpoons}} \text{CW}.$$

The Cluzel data on P_{CW} and F can then be transformed into data for λ_f and μ_f (Fig. 2C-D, dots). The transformation is based on the relations

$$\lambda_f(1-P_{CW}) = \mu_f P_{CW}, \quad F = \frac{2\lambda_f\mu_f}{\lambda_f+\mu_f}.$$

or equivalently,

$$\lambda_f = \frac{F}{2(1-P_{CW})}, \quad \mu_f = \frac{F}{2P_{CW}}.$$

This data can be fitted by requiring λ_f to be an increasing function of y_p and μ_f a decreasing function of y_p (Fig. 2). The fitting in [33] leads to

$$\begin{aligned} \lambda_f &= a_1 \exp(b_1 Y_p), \\ \mu_f &= a_2 \exp\big(-(b_2 - Y_p)^4/c\big), \end{aligned} \tag{6}$$

where a_1, b_1, a_2, b_2 and c are constants given in the caption of Fig. 2. Please note that these fitting results (solid curves) are much better than the original fitting method suggested in [32], which fits P_{CW} by a Hill function with hill coefficient 10.3 and $K_m = 3.1\mu$M and the derivative of the function for F (dashed curves).

To calculate the cell-level rates λ and μ, one way is to use a voting process: assume that all the flagella of a cell rotate independently and if the majority of them rotate CCW simultaneously then the cell runs forward, otherwise it tumbles in place [19]. In reality different flagella can interact with each other through the surrounding fluid, and the significance of the hydrodynamic interaction needs to be investigated in the future.

Assume that each cell has n_f flagella and in order for a cell to "run" at least w flagella are needed to rotate CCW simultaneously. The probability of having exactly i flagella rotating CCW is

$$P_{CCW}^i = \binom{n_f}{i} \left(\frac{\mu_f}{\lambda_f+\mu_f}\right)^i \left(\frac{\lambda_f}{\lambda_f+\mu_f}\right)^{n_f-i}. \tag{7}$$

The probability for the cell to be in the run and tumble states are given by

$$P_{run} = \sum_{i=w}^{n_f} P_{CCW}^i, \quad P_{tumble} = 1 - P_{run}. \tag{8}$$

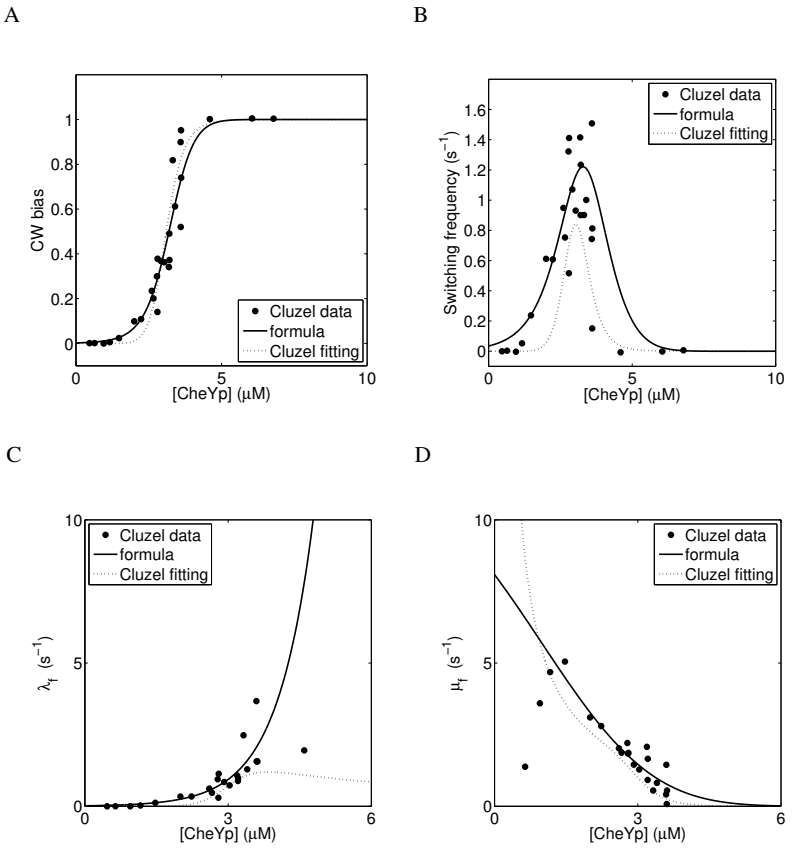

Fig. 2 Parameter fitting for the transition rates λ_f and μ_f as a function of CheYp (y_p). The dots are from experimental data extracted from Fig. 2 in [32]. The solid lines are calculated using the formula (6). Parameters: $a_1 = 0.0174001s^{-1}$, $b_1 = 1.32887\mu M^{-1}$, $a_2 = 12.0809s^{-1}$, $b_2 = -5.83762\mu M$, $c = 2892.12$. The dotted lines are calculated using the original fitting method suggested in [32].

The probability for multiple flagella switching rotation simultaneously at a specific time is much smaller than that for a single one. Hence, the transition from run to tumble primarily occurs when the cell has exactly w flagella rotating CCW and one of them switches to CW, i.e.,

$$\lambda = w\lambda_f \cdot \frac{P_{CCW}^w}{P_{run}}. \tag{9}$$

Similar argument leads to

$$\mu = (n_f - w + 1)\mu_f \cdot \frac{P_{CCW}^{w-1}}{P_{tumble}}. \tag{10}$$

Fig. 3 plots these rates determined with $n_f = 8$ and $w = 5$ and the time fraction that a cell spent running. It shows that the multi-flagella voting process help increase the sensitivity of the cell movement to intracellular CheYp level. It also showed that if the internal CheYp is perturbed far away from its baseline level ($\sim 3\mu$M), then the cell can be locked in the run or tumble state.

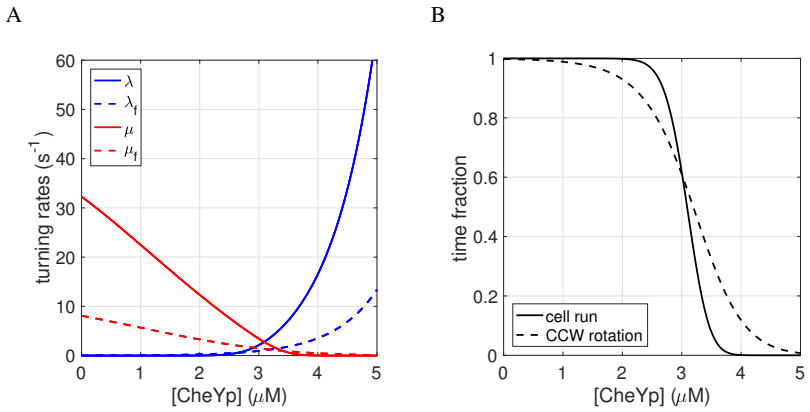

Fig. 3 A. The transition rates λ and μ as a function of CheYp determined by the voting process. B. Time fraction of cell running and flagella CCW rotation. Parameters: $n_f = 8$, $w = 5$.

3.2 Intracellular signaling modeled by an internal ODE system

Extensive effort has been put into modeling the intracellular chemotactic signaling of *E. coli* in the past 50 years, and the hand-in-hand interplay between experiments and modeling has led to profound quantitative understanding of the signaling dynamics (see reviews [34, 35]). These models usually adopt a system of ODEs to track the concentrations of intracellular proteins over time.

$$\frac{\mathrm{d}\mathbf{y}}{\mathrm{d}t} = \mathbf{f}\big(\mathbf{y}, S(\mathbf{x},t)\big), \tag{11}$$

Here $\mathbf{x} \in \mathbb{R}^N$ is the cell position, and $S(\mathbf{x},t)$ is the extracellular signal along the cell trajectory. To simulate a large population of cells, often a simplified ODE model was used for intracellular signaling instead. A key requirement of the model is that it must contain one variable that demonstrates the fast excitation and slow adaptation behavior as of CheYp. The intracellular CheYp concentration y_p is either an explicit equation in the system or represented as a function of the variable $\mathbf{y}$. In either case, one has

$$y_p = y_p(\mathbf{y}). \tag{12}$$

3.2.1 A cartoon model

The simplest dynamical system of this kind is the linear cartoon model used in [36, 37],

$$\begin{aligned} \frac{dy_1}{dt} &= \frac{S - y_1 - y_2}{t_e}, \\ \frac{dy_2}{dt} &= \frac{S - y_2}{t_a}, \end{aligned} \tag{13}$$

where $t_e \ll t_a$ are the excitation and adaptation time constants. Here y_1 is the variable that excites and fully adapts to its steady state 0 after a step signal change, and y_p can be identified as $-y_1$. This cartoon model has facilitated the development of multiscale methods to derive PDE models for cell population dynamics, which will be discussed in Sec 4.

3.2.2 A coarse-grained model

A conceptual model that incorporates the main structure of the excitation-adaptation network was introduced in [38]. The wiring diagram is given in Fig. 4A. S is the external signal measured by the fraction of receptor occupancy. E is the excitation process representing the phosphorylation of CheY by CheA_p. A is the adaptation process representing the phosphorylation of CheB by CheA_p. The reaction between E and A can be identified as the regulation of CheA activity by CheB_p through demethylation.

Denote the concentrations of E and A by y_1 and y_2. Using mass action kinetics, one has

$$\begin{aligned} \frac{dy_1}{dt} &= k_0 + k_s S - \mu_e y_1 y_2, \\ \frac{dy_2}{dt} &= k_0 + k_s S - \mu_a y_2. \end{aligned} \tag{14}$$

Given a step signal change, y_1 changes rapidly and adapts slowly to its pre-stimulus level (Fig. 4B). In this model, y_p can be identified as $-y_1$.

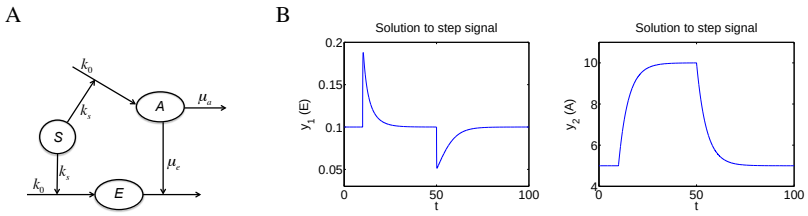

Fig. 4 The coarse-grained model. (A) The wiring diagram. (B) Solution of the model given step changes of the signal from 0 to 1 at $t = 10$ and from 1 to 0 at $t = 50$. Parameters used are non-dimensional: $k_0 = 1$, $k_s = 1$, $\mu_a = 0.2$, $\mu_e = 2$. Reproduced from [38] with permission.

3.2.3 A detailed model for *E. coli* chemotaxis

A comprehensive model for *E. coli* intracellular signaling was introduced to study cell population dynamics in [38]. The model is based on the full signaling network in Fig. 1 and a simplified version of trimers-of-dimers model proposed in [11] using quasi-steady state approximations of fast reactions and mean field approximations of the methylation level of the receptors.

Denote the mean methylation level of the chemoreceptors by m and the external signal concentration by S. The equation of m is governed by the methylation and demethylation reactions mediated by CheR (R) and CheB$_p$ (B_p),

$$\frac{\mathrm{dm}}{\mathrm{dt}} = k_R R\Big(1 - A(m,S)\Big) - k_{Bp} B_p A(m,S). \tag{15}$$

Here $A(m,S)$ is the mean receptor activity

$$A(m,S) = \frac{1}{1+\exp\left[N_r f(m,S)\right]}, \tag{16}$$

with

$$f(m,S) = \alpha(m_0 - m) + \log(1+S/K_i) - \log(1+S/K_a). \tag{17}$$

CheR concentration R is given by

$$R = \frac{R_t}{1+K_R T_t (1-A(m,S))}. \tag{18}$$

CheB$_p$ concentration B_p is implicitly given by a system of algebraic equations of B_p, Y_p (concentration of CheY$_p$) and T_p (concentration of CheAp-associated receptors) obtained by assuming quasi-steady states of these proteins,

$$\begin{aligned} k_A\Big(T_t A(m,S) - T_p\Big) - k_Y Y T_p - k_B B T_p &= 0, \\ k_Y Y T_p - \mu_Y Y_p - k_Z Z Y_p &= 0, \\ k_B B T_p - \mu_B B_p &= 0, \end{aligned} \tag{19}$$

where

$$\begin{aligned} Y &= \frac{Y_t - (1+K_Z Z) Y_p}{1+K_Y T_p}, \\ Z &= \frac{z}{1+K_Z Y_p}, \\ B &= \frac{B_t - (1+K_{Bp} T_t A(m)) B_p}{1+K_B T_p}. \end{aligned} \tag{20}$$

In this model y_p is simply given by the CheYp concentration Y_p. The function $A(m,S)$ and the solution subject to a step signal change is plotted in Fig. 5. A sample code of this model can be obtained online at [39].

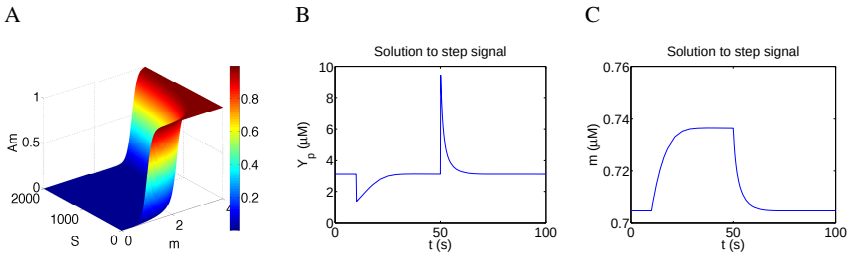

Fig. 5 The detailed model for *E. coli* chemotaxis. A: the function $A(m,S)$. B and C: solution of Y_p and m given step changes of the signal from 0 to 1 μM at $t = 10$ s and from 1 μM to 0 at $t = 50$ s. Parameter used: $m_0 = 1$, $\alpha = 1.7$, $K_i = 18$, $K_a = 3$, $N_r = 6$, $Y_t = 18\mu$M, $B_t = 2\mu$M, $R_t = 0.3\mu$M, $Z_t = 1.1\mu$M, $T_t = 5/3\mu$M, $k_R = 3.82\times10^{-2}\text{s}^{-1}$, $k_{Bp} = 3.25\text{s}^{-1}$, $k_A = 100\text{s}^{-1}$, $k_Y = 130\mu\text{M}^{-1}\text{s}^{-1}$, $k_B = 7.5\mu\text{M}^{-1}\text{s}^{-1}$, $k_Z = 8.45\mu\text{M}^{-1}\text{s}^{-1}$, $\mu_Y = 0.1\text{s}^{-1}$, $\mu_B = 1\text{s}^{-1}$, $K_Z = 1\mu\text{M}^{-1}$, $K_Y = 0.65\mu\text{M}^{-1}$, $K_{Bp} = 6.5\mu\text{M}^{-1}$, $K_B = 0.25\mu\text{M}^{-1}$, $K_R = 0.15\mu\text{M}^{-1}$. Reproduced from [38] with permission.

4 From individual-based models to PDE models

PDE models have been used extensively to describe chemotactic movement of cell populations in biological and biomedical applications [40, 41, 42, 43, 44, 45]. A fundamental challenge faced by modelers is to determine under what conditions these models provide a good approximation to the underlying biological process and how to accurately estimate the parameters in the PDEs. To address this problem, mathematical analysis must be developed to elucidate the connections of PDE models and individual-based models.

Significant progress has been made along this line in the context of bacterial chemotaxis, the simplest form of chemotaxis among all cell types. Macroscopic PDEs have been derived from the individual-based models described in Sec. 3.

4.1 The Patlak-Keller-Segel equation for chemotaxis in small signal gradients

When the cell density is low, the most popular PDE approach for chemotaxis is to use the classical Patlak-Keller-Segel (PKS) equation (or a variation of it) to describe the evolution of the cell density

$$\frac{\partial n}{\partial t} = \nabla\cdot\Big(D_n\nabla n - \chi n\nabla S\Big), \tag{21}$$

where $n = n(\mathbf{x},t)$ is the cell density, $S = S(\mathbf{x},t)$ is the signal concentration, D_n is the effective diffusion coefficient, and $\chi = \chi(S,\nabla S,n,\ldots)$ is the chemotactic sensitivity. Similar equations have also been used to describe cell movement towards other signals, e.g., mechanical signals, light and heat.

Eqn (21) has been formally derived for bacterial chemotaxis. The underlying assumption is that the external signal $S(\mathbf{x},t)$ changes slow enough along cell trajectories such that intracellular signaling is close to equilibrium. A primitive form of this condition was first introduced in [36, 37] as the "shallow gradient assumption" and later elaborated in [38] as the "small signal variation assumption". This assumption leads to time scale separation of intracellular signaling and external signal variation, which justifies the application of perturbation method with the small parameter being the ratio of different time scales.

The derivation in early works [46, 47, 48, 49] does not incorporate intracellular signaling explicitly; instead, the turning rates of the velocity jump processes depend directly on the external signal. Built upon these methods, the derivation in more recent works incorporated intracellular signaling by ODE systems described in Sec 3.2 [36, 37, 50, 38].

4.1.1 Derivation with intracellular dynamics given by the cartoon model (13)

In [36, 37], Eqn. (21) was derived from the individual-based model with the linear cartoon model (13) for intracellular signaling and the linear turning rate

$$\lambda = \lambda_0 - a_1 y_1$$

for cell movement. The key ideas of the derivation is presented below.

Consider cell movement in 1D and assume that the external signal does not change over time, i.e., $S = S(x)$. Let $z = y_2 - S$ and pass y_1 to its quasi-steady state, then

$$\begin{aligned} \frac{\mathrm{d}z}{\mathrm{d}t} &= -\frac{z}{t_a} \mp s_0 S_x, \\ \lambda &= \lambda_0 + a_1 z, \end{aligned} \tag{22}$$

where minus should be used for right-moving cells and plus should be used for left-moving cells.

Let $p^{\pm} = p^{\pm}(x,z,t)$ be the density of cells at position x with internal state z and velocity $\pm s_0$ at time t. Assume that cells are unbiased in choosing new directions of movement after tumbling, then one has

$$\begin{aligned} \frac{\partial p^+}{\partial t} + s_0 \frac{\partial p^+}{\partial x} + \frac{\partial}{\partial z}\left[\left(-\frac{z}{t_a} - s_0 S_x(x)\right) p^+\right] &= \frac{1}{2}(\lambda_0 + a_1 z)\left(-p^+ + p^-\right), \\ \frac{\partial p^-}{\partial t} - s_0 \frac{\partial p^-}{\partial x} + \frac{\partial}{\partial z}\left[\left(-\frac{z}{t_a} + s_0 S_x(x)\right) p^-\right] &= \frac{1}{2}(\lambda_0 + a_1 z)\left(p^+ - p^-\right). \end{aligned} \tag{23}$$

The macroscopic cell density is given by

$$n(x,t) = \int_{\mathbb{R}} (p^+ + p^-)\mathrm{d}z.$$

To obtain approximating equations for $n(x,t)$, one needs to integrate the system (23) over the internal variable z. Denote

$$\begin{aligned} j(x,t) &= \int_{\mathbb{R}} s_0(p^+ - p^-)\mathrm{d}z, \\ n_k(x,t) &= \int_{\mathbb{R}} z^k(p^+ + p^-)\mathrm{d}z, \\ j_k(x,t) &= \int_{\mathbb{R}} z^k s_0(p^+ - p^-)\mathrm{d}z, \quad k \geq 1, \end{aligned}$$

where $n(x,t)$ and $j(x,t)$ are the macroscopic cell density and flux.

Taking the sum and difference of the two components of (23) and integrating over z, one obtains

$$\begin{aligned} &\frac{\partial n}{\partial t} + \frac{\partial j}{\partial x} = 0, \\ &\frac{\partial j}{\partial t} + s_0^2 \frac{\partial n}{\partial x} = -\lambda_0 j - a_1 j_1, \end{aligned} \tag{24}$$

Multiplying (23) by z and then performing the same calculations, one obtains

$$\begin{aligned} &\frac{\partial n_1}{\partial t} + \frac{\partial j_1}{\partial x} = -S_x(x) j - \frac{1}{t_a} n_1, \\ &\frac{\partial j_1}{\partial t} + s_0^2 \frac{\partial n_1}{\partial x} = -s_0^2 S_x(x) n - \left(\lambda_0 + \frac{1}{t_a}\right) j_1 - a_1 j_2, \end{aligned} \tag{25}$$

The moment-flux system (24) and (25) is not closed because the 2nd-order moment j_2 in (25) is unknown. To obtain a closed moment-flux system, j_2 must be estimated as a function of lower-order moments. If we approximate y_2 by its quasi-steady state in Eqn (13), then $z = y_2 - S(x) \approx 0$, leading to the moment closure assumption

$$j_2 = \int_{\mathbb{R}} z^2 s_0(p^+ - p^-)\mathrm{d}z \approx 0. \tag{26}$$

This estimation is justified if the external signal changes slowly along the cell trajectory, in which case the internal states of the cells are only slightly perturbed away from equilibrium. The closed moment-flux system (24) - (26) represents a macroscopic model for the bacterial population dynamics.

Using the diffusion space and time scale, the system (24)-(26) can be rewritten as

$$\begin{aligned} &\varepsilon^2 \frac{\partial n}{\partial t} + \varepsilon \frac{\partial j}{\partial x} = 0, \\ &\varepsilon^2 \frac{\partial j}{\partial t} + \varepsilon s_0^2 \frac{\partial n}{\partial x} = -\lambda_0 j - a_1 j_1, \\ &\varepsilon^2 \frac{\partial n_1}{\partial t} + \varepsilon \frac{\partial j_1}{\partial x} = -\varepsilon S_x(x) j - \frac{1}{t_a} n_1, \\ &\varepsilon^2 \frac{\partial j_1}{\partial t} + \varepsilon s_0^2 \frac{\partial n_1}{\partial x} = -\varepsilon s_0^2 S_x(x) n - \left(\lambda_0 + \frac{1}{t_a}\right) j_1, \end{aligned} \tag{27}$$

Here the small parameter ε can be regarded as the ratio of the time scale for intracellular adaptation t_a and the time scale for detected external signal variation $T_s = a_1 s_0 S_x/\lambda_0$.

Using the Hilbert expansion $u(x,t) = \sum_{j=0}^{\infty} \varepsilon^j u^j(x,t)$ for each variable and matching terms with the same order of ε, the 1D form of Eqn. (21) was derived from (27) for $n^0(x,t) = n(x,t) + \mathscr{O}(\varepsilon)$:

$$\partial_t n^0 = \partial_x \Big(D_n \partial_x n^0 - \chi n^0 \partial_x S \Big), \tag{28}$$

where

$$D_n = s_0^2/\lambda_0, \qquad \chi = \frac{a_1 s_0^2 t_a}{\lambda_0(1+\lambda_0 t_a)}. \tag{29}$$

Alternative moment closure methods were also suggested in [36] based on quasi-steady state approximations of z. Replacing one or both z in the definition of j_2 by its quasi-steady state $z_{qss} = \mp s_0 S_x(x) t_a$, "-" for right-moving cells (p^+) and "+" for left-moving cells (p^-), one obtains

$$j_2 \approx -s_0^2 S_x(x) t_a n_1, \tag{30}$$

or

$$j_2 \approx s_0^2 S_x(x)^2 t_a^2 j. \tag{31}$$

Under these closure assumptions, the system (24), (25) reduces to the same PKS equation.

In [50], a new method was developed to accommodate a nonlinear turning frequency given by the expansion

$$\lambda(z) = \lambda_0 + \sum_{i=1}^{\infty} a_i z^i. \tag{32}$$

The derivation did not involve any moment closure step, but instead employed regular perturbation to the infinite moment system for n, j, n_k and j_k with $k \geq 1$ on the diffusion space and time scale. Perturbation of an infinite moment system involves the inversion of an infinite matrix operator that is not feasible in general. In this case, a special technique was developed utilizing the structure of the equations. With these extensions, the resulting PKS model has the following parameters

$$D_n = \frac{s_0^2}{N\lambda_0}, \qquad \chi = \frac{a_1 s_0^2 t_a}{N\lambda_0(1+\lambda_0 t_a)}, \tag{33}$$

where $N = 3$ is the space dimension.

4.1.2 Derivation with the general ODE model (11) for cell signaling

In [38], mathematical analysis was developed to derive the PKS equation from individual-based models with cell signaling given by the general ODE system (11).

Given the base model for cell movement, Equation (21) was derived with the following formula for D_n and χ

$$\begin{aligned} D_n &= \frac{s_0^2}{N\lambda_0(1-\psi_d)}, \\ \chi &= \frac{s_0^2}{N\lambda_0}\left[(\nabla_{\mathbf{y}}\lambda)|_{\mathbf{y}=\bar{\mathbf{y}}(S)}\cdot\left(\lambda_0(1-\psi_d)I_q-(\nabla_{\mathbf{y}}\mathbf{f})|_{\mathbf{y}=\bar{\mathbf{y}}(S)}\right)^{-1}\frac{\mathrm{d}\bar{\mathbf{y}}(S)}{\mathrm{d}S}\right]. \end{aligned} \tag{34}$$

Here N is the space dimension, $\lambda=\lambda(y_p(\mathbf{y}))$, $\lambda_0=\lambda(\bar{\mathbf{y}})$, $\bar{\mathbf{y}}(S)$ is the adapted state satisfying $\mathbf{f}(\bar{\mathbf{y}},S)=0$, I_q is the $q\times q$ identity matrix, q is the dimension of the internal variable, and ψ_d is the index of directional persistence given by

$$\psi_d=\left(\mathbf{v}'\cdot\int_V T(\mathbf{v},\mathbf{v}')\mathbf{v}\mathrm{d}\mathbf{v}\right)\Big/ s_0^2. \tag{35}$$

The derivation was based on a small signal variation assumption, which essentially assumes $t_a \ll T_s$, where t_a is the adaptation time scale intrinsically determined by the intracellular signaling network, and T_s is the time scale for the external signal variation interpreted by a cell. For the general ODE model, t_a and T_s can be approximated as

$$t_a \sim 1\Big/\min_{0\le S\le S_{\max}}\left|\sigma_m\left((\nabla_{\mathbf{y}}\mathbf{f})|_{\mathbf{y}=\bar{\mathbf{y}}(S)}\right)\right|, \tag{36}$$

$$T_s \sim 1\Big/\max_{\substack{0\le S\le S_{\max}\\ \mathbf{v}\in V}}\lambda_0^{-1}\left\|\nabla_{\mathbf{y}}\lambda|_{\mathbf{y}=\bar{\mathbf{y}}(S)}\right\|\cdot\left\|\frac{\mathrm{d}\bar{\mathbf{y}}(S)}{\mathrm{d}S}\dot{S}\right\|, \tag{37}$$

where σ_m takes the maximum real part of the eigenvalues of a matrix.

The formula (34) provides a means to embed the detailed biochemistry of intracellular signaling into macroscopic PDEs for the population. It is the first set of general formulas that represent the quantities D_n and χ in terms of the structure and kinetics of the intracellular signaling network. When applied to the cartoon model (13), it reduces to the same formula as in previous works. When applied to the coarse-grained model (14), it leads to a logarithmic chemotactic sensitivity that depends on the signal S

$$\chi=\frac{\chi_0}{S+\alpha_0}. \tag{38}$$

In other words, the macroscopic drift of the population is proportional to the gradient of the logarithm of the signal

$$\mathbf{u}_s\equiv\chi\nabla S=\nabla\log(S+\alpha_0). \tag{39}$$

The logarithmic sensing mechanism was observed experimentally in [51]. These analyses suggest that the origin of the logarithmic sensing mechanism is the structure of the intracellular network [38].

When applied to the detailed model (15)-(20), the general formula predicted a logarithmic sensitivity with $\chi_0 = 9.50 \times 10^{-2}$mm/s and $\alpha_0 = 17.67\mu$M, comparable with experimental measurements. Due to the complicated form of the intracellular dynamics, the formula (34) was evaluated numerically with the derivatives approximated using a fourth-order accurate scheme and then fitted using the function (38) (Fig 6).

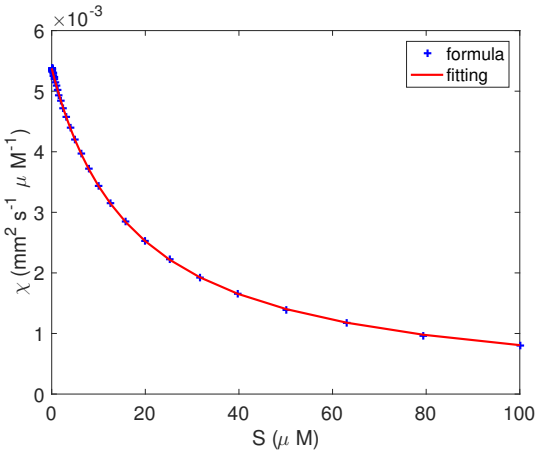

Fig. 6 Logarithmic sensitivity of *E. coli* predicted by the individual-based model with (15)-(20). The blue crosses are calculated using numerical approximations of the formula (34). The red line is the best fitting to the function (38). Parameters used: $\chi_0 = 9.50 \times 10^{-2}$mm/s, $\alpha_0 = 17.67\mu$M.

4.1.3 Limitations of PKS models

The PKS equation (21) provides an accurate approximation of the individual-based model when the external signal changes slowly along cell trajectories, but breaks down when the external signal changes fast, regardless of the form of the intracellular dynamics. This was shown by extensive numerical comparisons of the cell density dynamics predicted by the PKS equation and the corresponding individual-based model using different kinds of signal functions [38, 52]. PDE models derived in [53] have similar limitations as the PKS model.

Consider cell movement in a domain $x \in [0,8]$ mm with a static exponential ramp signal

$$S = \begin{cases} e^{a(x-1)} & 0 \le x \le 4, \\ e^{3a} & 4 < x \le 8. \end{cases} \tag{40}$$

Assume that initially cells form an aggregate in the region $x \in [1,2]$, and set the initial cell distribution to be

$$n(x,0) = \frac{3\pi}{4}\left|\sin(\pi x)\right|^3 \chi_{1<x<2}, \tag{41}$$

where $\chi_{1<x<2}$ is the characteristic function. Let

$$\lambda = \lambda_0 + \tanh\Big(b(Y_p(m) - \bar{Y}_p)\Big), \quad T(\mathbf{v},\mathbf{v}') = \frac{1}{|V|}, \qquad V = s_0 \partial B_0^1. \tag{42}$$

where $\lambda_0 = 1\mathrm{s}^{-1}$, $b = 5\mathrm{s}^{-1}\mu\mathrm{M}^{-1}$ and $s_0 = 20\mu\mathrm{m/s}$.

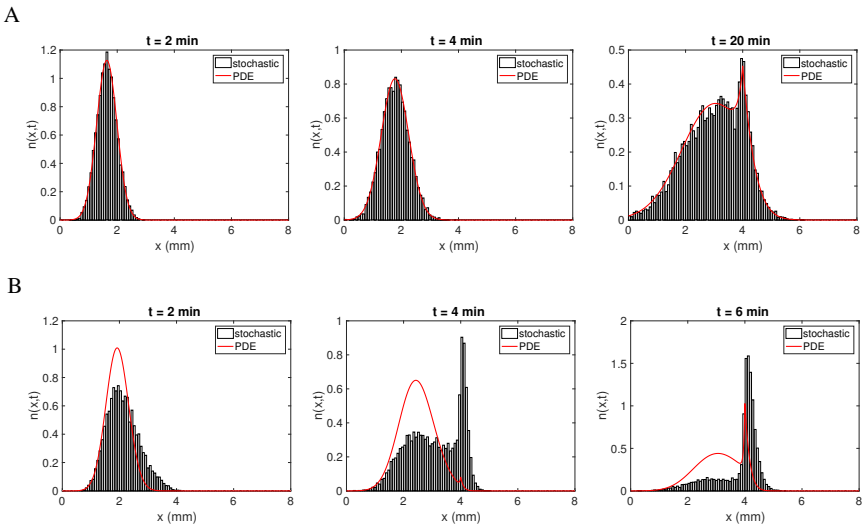

Fig. 7 Comparison of the PKS equation with the underlying individual-based model for bacterial chemotaxis in small signal gradient with $a = 0.2mm^{-1}$ (A) and large signal gradient with $a = 0.5mm^{-1}$ (B). Bars: stochastic simulations of the individual-based model with (15)-(20). Curves: solutions of the corresponding PKS model.

Fig. 7 plots the cell density dynamics predicted by the individual-based model with (15)-(20) and the corresponding PKS model. If the signal gradient is small ($a = 0.2mm^{-1}$), the two approaches match tightly (Fig. 7A); but if the signal gradient becomes large ($a = 0.5mm^{-1}$), the two approaches deviate significantly (Fig. 7B). The latter situation often occurs in self-organized population dynamics [54]. A key feature when the PKS approximation breaks down is the fat distribution of the intracellular states as shown in Fig. 8.

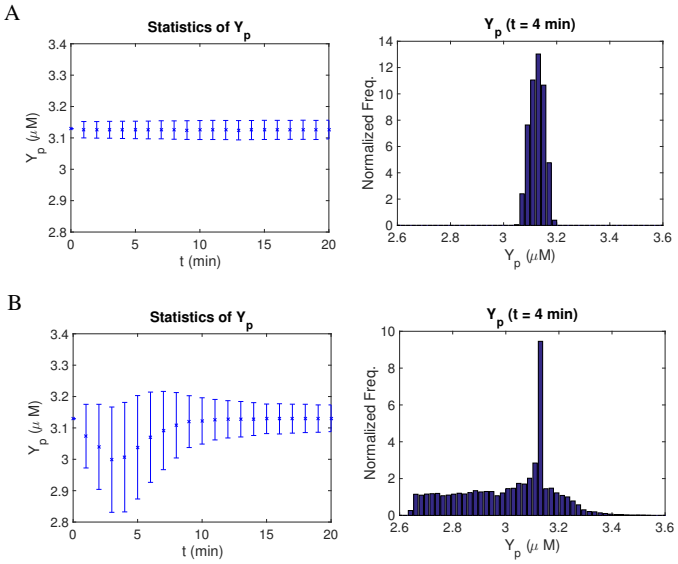

Fig. 8 Statistics of intracellular CheYp given small signal gradient with $a = 0.2mm^{-1}$ (A) and large signal gradient with $a = 0.5mm^{-1}$ (B). Left: mean and standard deviation of y_p over the whole population as a function of time. Right: distribution of y_p at $t = 4$ min.

4.2 Moment-flux models for chemotaxis in large signal gradients

When cells are exposed to large signal gradient, their intracellular state can be far from steady state and broadly distributed. Macroscopic PDE models for such situations must include information on the distribution of the intracellular states in order to accurately describe the population dynamics.

In [52], a hierarchy of moment-flux models that are suitable for bacterial chemotaxis in large gradient were derived from the individual-based model with the cartoon intracellular dynamics (13) and nonlinear turning rate (32). The models consist of a system of hyperbolic equations for n, j and several internal-state moments n_k and j_k with $k \leq K$. The moments n_k and j_k enclose the distribution of the internal state and its deviation from equilibrium.

Consider the example with cell signaling described by the simplified cartoon model (22) and cell movement subject to a time-independent signal. Multiplying (23) by 1 and z^k/k for all $k \geq 1$, integrating over z, and taking the sum and difference of the two components, we obtain (24) and the following moment equations

$$\begin{aligned} &\frac{1}{k}\frac{\partial n_k}{\partial t} + \frac{1}{k}\frac{\partial j_k}{\partial x} = \left[-S_x j_{k-1} - \frac{1}{t_a} n_k\right], \qquad k \geq 1 \\ &\frac{1}{k}\frac{\partial j_k}{\partial t} + \frac{s_0^2}{k}\frac{\partial n_k}{\partial x} = \left[-s_0^2 S_x(x) n_{k-1} - \frac{1}{t_a} j_k\right] - \frac{1}{k}\left(\lambda_0 j_k + a_1 j_{k+1}\right), \; k \geq 1. \end{aligned} \tag{43}$$

The system for $k = 1$ is identical to (25).

The k-th order moment equations (43) have the factor $1/k$ in all terms except the terms in the square brackets, which suggests that high-order moments in z equilibrate relatively fast. The moment closure method in [52] is to pick an integer K large enough such that $1/(K+1) \ll 1$ and set

$$\begin{aligned} -S_x(x)j_{k-1} - \frac{1}{t_a}n_k = 0 \qquad \forall k > K, \\ -s_0^2 S_x(x)n_{k-1} - \frac{1}{t_a}j_k = 0 \qquad \forall k > K. \end{aligned} \tag{44}$$

This assumption is equivalent to setting

$$j_{K+1} = -s_0^2 S_x(x) t_a n_K. \tag{45}$$

With this approximation, the infinite system (24) and (43) reduces to a closed moment system of moment equations for $(n, j, n_1, j_1, \cdots, n_K, j_K)^T$.

Numerical simulations showed that as K increases, the moment-flux models become more accurate in approximating the population dynamics governed by the individual-based model (Fig. 9). The models with $K = 3$ and 4 show a tight match to the individual-based model, while the PKS equation and the moment-flux models with $K = 1$ deviate from the individual-based model significantly. Note that the moment closure (45) with $K = 1$ reduces to the moment closure (30) which was used for the case with small signal gradient. Because the number of equations of the model $(2K+2)$ increases with K, it is desirable to use K as small as possible to reduce computational cost.

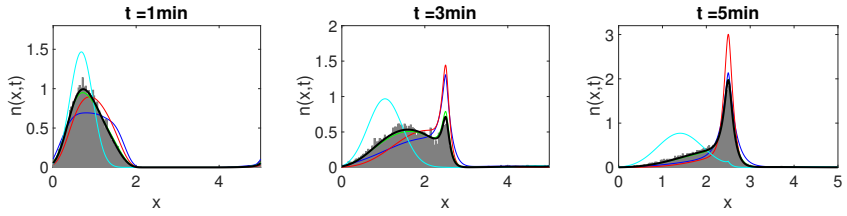

Fig. 9 Comparison of the moment-flux model, the PKS model and the underlying individual-based model with (22). The signal is given by $S(x) = \mu L/2 - \mu|x - L/2|$ with $L = 5$ mm and $\mu = 4.5$, which does not satisfy the small signal variation assumption. The gray bar plot is a single realization of the individual-based model with 10^4 cells. The blue, red, green and black curves are the numerical solutions of the moment-flux models with order $K = 1, 2, 3, 4$. The cyan curve is the solution of the PKS model.

4.3 Open problems

There are several open problems raised by previous multiscale analysis. The moment-flux models in [52] were derived using the linear cartoon model for intracellular signaling. The method needs to be extended to include intrinsic nonlinearities of the intracellular dynamics, e.g., as in (14) or (15)-(20). For cases in which the signal gradient only becomes large in part of the domain, hybrid methods that bridge individual-based models and PDE models can be developed. This is desirable especially in 3D, in which case simulations of the hyperbolic moment-flux models become very time-consuming.

5 Summary

This chapter summarizes the multiscale modeling framework used for bacterial chemotaxis and the major breakthroughs in deriving PDE models from individual-based models in this context. Analyses and simulations revealed that the PKS equation is accurate in approximating the population dynamics when cell movement is subject to small signal gradients, but it breaks down if the signal gradient becomes large. For the former case, detailed formulas were derived for the macroscopic parameters in the PKS equation in terms of measurable parameters that describe single cell signaling and movement. For the latter case, a hallmark is the broad distribution of the intracellular state over the whole population and alternative moment-flux PDE models could be used instead. This review is not to reiterate all relevant results in the literature, but written with enough detail so that it can be easily understood by researchers and graduate students with a diverse background. The hope is that the modeling methods developed for bacterial chemotaxis can be used or extended to address other multiscale problems in biology.

Acknowledgements I would like to thank Professor Hans Othmer and Professor Radek Erban for past collaboration and discussion on the described research. I also thank my student Clinton Durney for proofreading this chapter. This work was supported by the National Science Foundation under grant No. DMS-1312966 and NSF CAREER Award 1553637.

References

1. Sean P Cook, Charles J Brokaw, Charles H Muller, and Donner F Babcock. Sperm chemotaxis: egg peptides control cytosolic calcium to regulate flagellar responses. *Developmental biology*, 165(1):10–19, 1994.
2. Robert F Diegelmann, Melissa C Evans, et al. Wound healing: an overview of acute, fibrotic and delayed healing. *Front Biosci*, 9(1):283–289, 2004.
3. P. Friedl and D. Gilmour. Collective cell migration in morphogenesis, regeneration and cancer. *Nat Rev Mol Cell Biol*, 10(7):445–457, Jul 2009.

4. G. Pandey and R. K. Jain. Bacterial chemotaxis toward environmental pollutants: role in bioremediation. *Appl Environ Microbiol*, 68(12):5789–5795, Dec 2002.
5. J. P. Armitage, T. P. Pitta, M. A. Vigeant, H. L. Packer, and R. M. Ford. Transformations in flagellar structure of rhodobacter sphaeroides and possible relationship to changes in swimming speed. *J Bacteriol*, 181(16):4825–4833, Aug 1999.
6. K. J. Duffy and R. M. Ford. Turn angle and run time distributions characterize swimming behavior for pseudomonas putida. *J Bacteriol*, 179(4):1428–1430, Feb 1997.
7. C. V. Rao, J. R. Kirby, and A. P. Arkin. Design and diversity in bacterial chemotaxis: a comparative study in *Escherichia coli* and *Bacillus subtilis*. *PLoS Biol*, 2(2):E49, Feb 2004.
8. G. L. Hazelbauer. Bacterial chemotaxis: the early years of molecular studies. *Annu Rev Microbiol*, 66:285–303, Oct 2012.
9. D. E. Koshland. *Bacterial Chemotaxis as a Model Behavioral System*. Raven Press, New York, 1980.
10. H. C. Berg. *Random Walks in Biology*. Princeton University Press, 1983.
11. X. Xin and H. G. Othmer. A "trimer of dimers"-based model for the chemotactic signal transduction network in bacterial chemotaxis. *Bull Math Biol*, 74(10):2339–2382, Oct 2012.
12. J. Adler. Chemotaxis in bacteria. *SCIENCE*, 153:708–716, 1966.
13. Julius Adler. Effect of amino acids and oxygen on chemotaxis in escherichia coli. *Journal of bacteriology*, 92(1):121–129, 1966.
14. Julius Adler. Chemotaxis in bacteria. *Annual review of biochemistry*, 44(1):341–356, 1975.
15. E. O. Budrene and H. C. Berg. Complex patterns formed by motile cells of *Escherichia coli*. *Nature*, 349(6310):630–633, February 1991.
16. E. O. Budrene and H. C. Berg. Dynamics of formation of symmetrical patterns by chemotactic bacteria. *Nature*, 376(6535):49–53, 1995.
17. C. Xue, E. O. Budrene, and H. G. Othmer. Radial and spiral stream formation in *Proteus mirabilis* colonies. *PLoS Comput Biol*, 7(12):e1002332, 12 2011.
18. B. Franz, C. Xue, K. J. Painter, and R. Erban. Travelling waves in hybrid chemotaxis models. *Bull Math Biol*, 76(2):377–400, Feb 2014.
19. X. Xue, C. Xue, and M. Tang. The role of intracellular signaling in the stripe formation in engineered *E. coli* populations. *submitted*, 2017.
20. A Decoene, A Lorz, S Martin, B Maury, and M Tang. Simulation of self-propelled chemotactic bacteria in a stokes flow. In *ESAIM: proceedings*, volume 30, pages 104–123. EDP Sciences, 2010.
21. A. Decoene, S. Martin, and B. Maury. Microscopic modelling of active bacterial suspensions. *Mathematical Modelling of Natural Phenomena*, 6:98–129, 2011.
22. Robert Dillon, Lisa Fauci, and III Donald Gaver. A microscale model of bacterial swimming, chemotaxis and substrate transport. *Journal of Theoretical Biology*, 177(4):325 – 340, 1995.
23. Heather Flores, Edgar Lobaton, Stefan Méndez-Diez, Svetlana Tlupova, and Ricardo Cortez. A study of bacterial flagellar bundling. *Bulletin of Mathematical Biology*, 67(1):137–168, 2005.
24. J. P. Hernández-Ortiz, Ch. G. Stoltz, and M. D. Graham. Transport and collective dynamics in suspensions of confined swimming particles. *Physical Review Letters*, 95:204501, 2005. (doi:10.1103/PhysRevLett.95.204501).
25. J. P. Hernández-Ortiz, P. T. Underhill, and M. D. Graham. Dynamics of confined suspensions of swimming particles. *J. Phys.: Condens. Matter*, 21(20):204107, 2009.
26. S. D. Ryan, B. M. Haines, L. Berlyand, F. Ziebert, and I. S. Aranson. Viscosity of bacterial suspensions: Hydrodynamic interactions and self-induced noise. *Physical Review E*, 83(050904(R)), 2011.
27. S. D. Ryan, A. Sokolov, L. Berlyand, and I. S. Aranson. Correlation properties of collective motion in bacterial suspensions. *New Journal of Physics*, 15:105021, 2013.
28. H. G. Othmer, S. R. Dunbar, and W. Alt. Models of dispersal in biological systems. *J. Math. Biol.*, 26(3):263–298, 1988.
29. H. Othmer and C. Xue. The mathematical analysis of biological aggregation and dispersal: progress, problems and perspectives. In M. Lewis, P. Maini, and S. Petrovskii, editors, *Dispersal, individual movement and spatial ecology: A mathematical perspective*. Springer, 2013.

30. H. C. Berg and D. Brown. Chemotaxis in *Escherichia Coli* analyzed by three-dimensional tracking. *Nature*, 239:502–507, 1972.
31. R. M. Macnab. Sensing the environment: Bacterial chemotaxis. In R. Goldberg, editor, *Biological Regulation and Development*, pages 377–412, New York, 1980. Plenum Press.
32. P. Cluzel, M. Surette, and S. Leibler. An ultrasensitive bacterial motor revealed by monitoring signaling proteins in single cells. *Science*, 287:1652–1655, 2000.
33. Clinton H Durney. A two-component model for bacterial chemotaxis, 2013.
34. H. G. Othmer, X. Xin, and C. Xue. Excitation and adaptation in bacteria-a model signal transduction system that controls taxis and spatial pattern formation. *Int J Mol Sci*, 14(5):9205–9248, 2013.
35. M. J. Tindall, S. L. Porter, P. K. Maini, G. Gaglia, and J. P. Armitage. Overview of mathematical approaches used to model bacterial chemotaxis I: the single cell. *Bull Math Biol*, 70(6):1525–1569, Aug 2008.
36. R. Erban and H. G. Othmer. From individual to collective behavior in bacterial chemotaxis. *SIAM J. Appl. Math.*, 65(2):361–391, 2004.
37. R. Erban and H. Othmer. From signal transduction to spatial pattern formation in *E. coli*: A paradigm for multiscale modeling in biology. 3(2):362–394, 2005.
38. C. Xue. Macroscopic equations for bacterial chemotaxis: integration of detailed biochemistry of cell signaling. *J Math Biol*, 70(1-2):1–44, Jan 2015.
39. https://people.math.osu.edu/xue.41/pub.html.
40. C. S. Patlak. Random walk with persistence and external bias. *Bull. of Math. Biophys.*, 15:311–338, 1953.
41. E. F. Keller and L. A. Segel. Initiation of slime mold aggregation viewed as an instability. *J. Theor. Biol.*, 26:399–415, 1970.
42. E. F. Keller and L. A. Segel. Model for chemotaxis. *J. Theor. Biol.*, 30:225–234, 1971.
43. E. F. Keller and L. A. Segel. Traveling bands of chemotactic bacteria: A theoretical analysis. *J. Theor. Biol.*, 30:235–248, 1971.
44. Benoit Perthame. Pde models for chemotactic movements: parabolic, hyperbolic and kinetic. *Applications of Mathematics*, 49(6):539–564, 2004.
45. M. J. Tindall, P. K. Maini, S. L. Porter, and J. P. Armitage. Overview of mathematical approaches used to model bacterial chemotaxis II: bacterial populations. *Bull Math Biol*, 70(6):1570–1607, Aug 2008.
46. Mercedes A Rivero, Robert T Tranquillo, Helen M Buettner, and Douglas A Lauffenburger. Transport models for chemotactic cell populations based on individual cell behavior. *Chemical engineering science*, 44(12):2881–2897, 1989.
47. T. Hillen and H. G. Othmer. The diffusion limit of transport equations derived from velocity-jump processes. *SIAM J. Appl. Math.*, 61(3):751–775, 2000.
48. H. G. Othmer and T. Hillen. The diffusion limit of transport equations II: chemotaxis equations. *SIAM J. Appl. Math.*, 62:1222–1250, 2002.
49. F. A. C. C. Chalub, P. A. Markowich, B. Perthame, and C. Schmeiser. Kinetic models for chemotaxis and their drift-diffusion limits. *Monatshefte für Mathematik*, 142(1):123–141, 2004.
50. C. Xue and H. G. Othmer. Multiscale models of taxis-driven patterning in bacterial populations. *SIAM J. Appl. Math.*, 70(1):133–167, 2009.
51. Yevgeniy V. Kalinin, Lili Jiang, Yuhai Tu, and Mingming Wu. Logarithmic sensing in *Escherichia coli* bacterial chemotaxis. *Biophys J*, 96(6):2439–2448, Mar 2009.
52. C. Xue and X. Yang. Moment-flux models for bacterial chemotaxis in large signal gradients. *J Math Biol*, 73(4):977–1000, 2016.
53. J. E. Simons and P. A. Milewski. The volcano effect in bacterial chemotaxis. *Mathematical and Computer Modelling*, 53(7-8):1374–1388, 2011.
54. B. Franz, C. Xue, K. Painter, and R. Erban. Travelling waves in hybrid chemotaxis models. *Bull. Math. Biol.*, 2014.